Synthesis of severe lattice distorted MoS_2 coupled with hetero-bonds as anode for superior lithium-ion batteries

Liu, Yanyan; Zhang, Long; Wang, Hongqiang; Yu, Chuang; Yan, Xinlin; Liu, Qiunan; Xu, Bo; Wang, Li min

DOI
10.1016/j.electacta.2018.01.023

Publication date
2018

Document Version
Accepted author manuscript

Published in
Electrochimica Acta

Electrochimica Acta 262 (2018) 162–172

Contents lists available at ScienceDirect

Electrochimica Acta

journal homepage: www.elsevier.com/locate/electacta

Synthesis of severe lattice distorted MoS_2 coupled with hetero-bonds as anode for superior lithium-ion batteries

Yanyan Liu [a], Long Zhang [a, *], Hongqiang Wang [b], Chuang Yu [c], Xinlin Yan [d], Qiunan Liu [a], Bo Xu [a], Li-min Wang [a]

[a] State Key Laboratory of Metastable Materials Science and Technology, Yanshan University, Qinhuangdao, Hebei 066004, China
[b] College of Chemistry & Environmental Science, Hebei University, Baoding, Hebei 071000, China
[c] Department of Radiation Science and Technology, Delft University of Technology, Mekelweg 15, Delft 2629 JB, The Netherlands
[d] Institute of Solid State Physics, Vienna University of Technology, Wiedner Hauptstr. 8-10, 1040 Vienna, Austria

ARTICLE INFO

Article history:
Received 16 November 2017
Received in revised form
29 December 2017
Accepted 4 January 2018
Available online 4 January 2018

Keywords:
MoS_2
Polyethylene glycol
Oxygen-containing groups
Lattice distortion
Lithium-ion batteries

ABSTRACT

Exploration of advanced anode materials is a highly relevant research topic for next generation lithium-ion batteries. Here, we report severe lattice distorted MoS_2 nanosheets with a flower-like morphology prepared with PEG400 as additive, which acts not only as surfactant but importantly, also as reactant. Notably, in the absence of a carbon-related incorporation/decoration, it demonstrates superior electrochemical performance with a high reversible capacity, a good cycling stability, and an excellent rate capability, originated from the advantages of synthesized MoS_2 including enlarged interlayer spacing, 1T-like metallic behavior, and coupling of Mo–O–C (and Mo–O) hetero-bonds. PEG-assisted synthesis is believed applicable to other anode materials with a layered structure for lithium-ion batteries.

1. Introduction

Lithium ion batteries (LIBs) have been the most promising power source for electronic devices. With the intense development of smart devices and electric vehicles, further improvements of energy density, cycling life, and ability of fast charging/discharging are anticipated [1–3]. Graphitized carbon is currently served as a commercial negative electrode, but the low theoretical capacity (372 mAh g^{-1}) and the poor rate performance restrict its application in many fields [4,5]. Transition-metal sulfides have attracted tremendous attention to be used in LIBs because of their high theoretical capacity and relatively good electrochemical performance [6]. Among these materials, molybdenum disulfide (MoS_2) has been intensively investigated as one of the most promising next-generation anode materials for LIBs because of several advantages including [7–12]: (1) a high theoretical capacity of 670 mAh g^{-1}; (2) a layered structure with a large interlayer spacing of 0.62 nm and thus weak van der Waals forces between the S-Mo-S neighboring layers, which is beneficial to the intercalation of Li^+; (3) existence of 1T-like structure leading to metallic behavior to enhance the electrical conductivity; and (4) a low cost and easy fabrications.

However, there are also challenges in the development of MoS_2 anode toward high electrochemical performance such as a poor cycling stability and inferior rate capability, which can be accounted for the low intrinsic electrical conductivity between the S-Mo-S layers and structural deterioration due to the large volume expansion upon cycling [13]. So far lots of works have been focused on solving these issues [14–17]. One of the effective ways is to enlarge interlayer spacing of MoS_2 because it can not only accommodate more Li atoms to increase the specific capacity but also tolerate the lager volume expansion in the intercalation/deintercalation process so as to improve the structural stability [18]. The interlayer spacing can be expanded via intercalating or trapping foreign species for example, the cationic groups, the functional groups, and the polymer chains [7,9,18].

An environmental friendly nonionic surfactant polyethylene glycol (PEG) has been reported to be used as a surface dispersant agent and play a crucial role in the formation of nanostructure because of the binding effect. Abundant active oxygen atoms of PEG lead to a strong interaction between PEG chains and metal ions [19,20]. Therefore, PEG-assisted synthesis methods are widely used

* Corresponding author.
E-mail address: lzhang@ysu.edu.cn (L. Zhang).

https://doi.org/10.1016/j.electacta.2018.01.023
0013-4686/

for such as biomedical materials and solar cells [21–23]. To the best of our knowledge, so far there is no report on PEG-assisted synthesized MoS_2 as anode for LIBs. However, it is found that PEG accelerates the dispersion of precursors and prevents the agglomeration of MoS_2 nanoparticles during desulphurizing [24]. On the other hand, because of the interaction effect, oxygen-containing groups in PEG may insert into the interlayer spacing of MoS_2. This is beneficial to a high reversible capacity and excellent rate capability because the oxygen-containing groups may serve as a bridge between the S-Mo-S layers to facilitate the electron transfer, provide active sites for the reaction with Li^+, and play a supporting role to maintain the structural stability [25]. Therefore, it is highly motivated to synthesize MoS_2 as anode for LIBs using the PEG-assisted method.

In this work, an interlayer enlarged MoS_2 was prepared by a facile hydrothermal method using water plus the PEG400 additive as hydrothermal solvent. In addition to act as a surfactant to form flower-like MoS_2 nanosheets, the PEG400 addictive has several advantages due to incorporation of oxygen- and carbon-containing groups: (1) Evaluated from X-ray powder diffraction (XRD) and transmission electron microscope (TEM) measurements, the interlayer spacing was enlarged as wide as 1.0 nm. This value is significantly larger than that of bulk MoS_2 (0.62 nm). (2) Observed from the Fourier transform infrared spectra (FTIR) and X-ray photoelectron spectroscopy (XPS) data, Mo—O—C (and Mo—O) hetero-bonds were formed during hydrothermal processes. (3) Observed from Raman spectrum, MoS_2 nanosheets contain only few layers, thus demonstrating 1T-like metallic behavior. All these advantages enable MoS_2 prepared with PEG400 addictive demonstrating superior electrochemical performance compared to that prepared completely using water as solvent. Additionally, these advantages vanished after annealing MoS_2 at 550 °C, verifying the key role of the hetero-bonds incorporation on performance enhancements.

2. Experimental section

2.1. Synthesis of MoS_2 nanosheets

The MoS_2 nanosheets were prepared by a hydrothermal method. All the chemicals were used as received without further purification. First, 1.2 g sodium molybdate hexahydrate ($Na_2MoO_4 \cdot 2H_2O$, 99.95%, Aladdin) and 1.9 g thiourea (CH_4N_2S, 99%, Alfa Aesar) were dissolved in 60 mL distilled water (sample designated as MoS_2-H_2O) or in a mixture of 30 mL distilled water and 30 mL PEG400 (purchased from Alfa Aesar; sample designated as MoS_2-PEG) under magnetic stirring to form a homogenous solution. Then, the solution was transferred into a 100 mL Teflon-lined stainless-steel autoclave and maintained at 190 °C for 24 h. After the autoclave cooled to room temperature naturally, the products were collected by centrifugation, washed with distilled water, ethanol and acetone for several times and dried at 80 °C under vacuum. For comparison, MoS_2-PEG was annealed at 550 °C for 3 h under Ar flow (designated as MoS_2-PEG-A) to restore the ordered structure and remove the hetero-bonds.

2.2. Materials characterization

XRD was performed using a Rigaku D/MAX-2500/PC (Cu Kα, 40 kV 200 mA) from 5° to 70°. Morphological characterizations were taken with a scanning electron microscope (SEM, Hitachi S-4800 II FESEM) equipped with an energy dispersive spectrometry (EDS) instrument. TEM images were taken on a FEI Titan ETEM microscope. The XPS spectra were recorded by using a spectrometer with Al Kα radiation (ESCALAB 250 XI). The binding energy value of each element was corrected by C1s = 284.6 eV. Raman scattering measurements were performed using a Renishaw inVia system with a 532 nm excitation source. FTIR spectra were recorded in an E55 + FRA106 instrument (NICOLET-5700) at ambient temperature in the range from 4000 to 400 cm^{-1}. Differential scanning calorimetry (DSC) and thermogravimetric analysis (TGA) measurements were carried out on a Netzsch STA thermoanalyzer in an argon atmosphere.

2.3. Electrochemical characterization

The electrochemical performance of the MoS_2 electrodes was measured in CR2032 coin cells. The working electrode consists of active material (MoS_2-PEG, MoS_2-PEG-A, MoS_2-H_2O), acetylene black and Poly(vinylidene fluoride) (PVDF) with a mass ratio of 80:10:10, dissolved in N-methylpyrrolidinone (NMP). The resulting slurry was painted on a Cu foil and dried at 110 °C for 12 h under vacuum, and then cut into disks of 12 mm diameter. Li foil was used as the counter/reference electrode. 1 M LiPF6 dissolved in a mixture of ethylene carbonate (EC), ethyl methyl carbonate (EMC), and dimethyl carbonate (DMC) (1:1:1) was used as electrolyte with FEC (5 wt%) as addictive, and Celgard 2400 was used as the separator film. Finally, the cells were assembled in an Ar-filled glovebox. The galvanostatic charge and discharge measurements and rates performance were performed on an Arbin BT2000 system in a voltage range of 3 to 0.01 V at ambient temperature.

The specific capacity was calculated based on the weight of the active material, as much as 80 wt% weight of the electrode. Cyclic voltammetry (CV) measurements were tested on a Princeton P4000 electrochemical workstation at 0.1 mV s^{-1} in the voltage range from 3 to 0.01 V. Electrochemical impedance spectroscopy (EIS) was carried out on a Princeton P4000 electrochemical workstation in the frequency range of 100 KHz to 0.01 Hz at by applying a potential of 5 mV.

3. Results and discussion

3.1. Structural and physical properties

Fig. 1 shows the XRD profiles of MoS_2 using PEG400 as solvent before (MoS_2-PEG) and after (MoS_2-PEG-A) annealing and compared with that using H_2O (MoS_2-H_2O) as solvent. MoS_2-PEG demonstrates two specific new peaks at $2\theta = 8.7°$ (#1) and

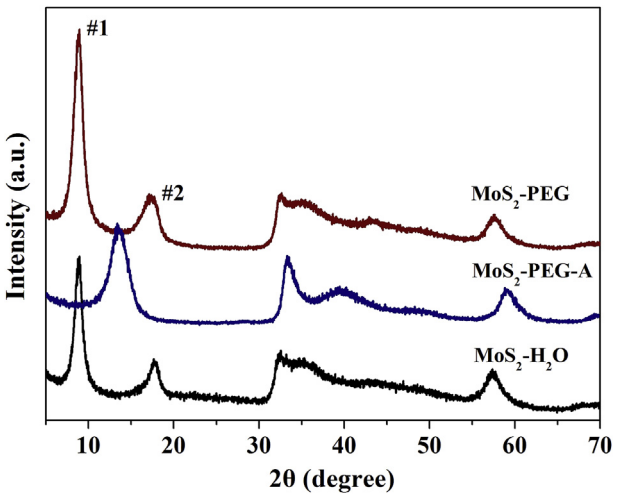

Fig. 1. XRD profiles of MoS_2-PEG before and after annealing at 550 °C and MoS_2-H_2O.

$2\theta = 17.4^\circ$ (#2) corresponding to the (00*l*) reflections, similar to 2H-MoS_2 but absence of the characteristic peak of 2H-MoS_2 at $2\theta = 14.4^\circ$ for (002) reflection, indicating the formation of a new graphene-like 2D structure, differing from 2H-MoS_2 [26]. Calculated from the Bragg equation with $d = 0.5\lambda/\sin(\theta)$, the interlayer distances of these two new peaks are *ca.* 1.0 and 0.5 nm, respectively. Compared with the d-spacing of 0.62 nm corresponding to the (002) plane of 2H-MoS_2, the enlarged d-spacing for the new peak at $2\theta = 8.7^\circ$ can be assigned to the intercalation of foreign atoms and/or functional groups into the spacing between the Mo-S layers. The peak at $2\theta = 17.4^\circ$ may represent the interlayer spacing between the MoS_2 layer and the foreign atom layer. The disappearance of (002) reflections indicates that the structure of such 2D MoS_2 contains only a few MoS_2 layers [27]. This result is verified by the microstructure observation from TEM (Fig. 2). A typical cluster of flower-like MoS_2 is shown in Fig. 2a. It can be obviously seen that the "petals" (nanosheets) are very thin since the electron beam can penetrates them despite of the overlap of the "petals". The nanosheet contains only a few MoS_2 layers with a distance of 0.97 nm (Fig. 2b) corresponding to the (00*l*) crystal plane. Moreover, a large amount of defects/distortions induced by the severe lattice distortion are observed, which is beneficial to stabilize the ultrathin MoS_2 nanosheets and generates more active unsaturated atoms because of the lowered surface energy [28]. The lattice spacing perpendicular to the (00*l*) plane is 0.27 nm, which is assigned to the (100) crystal plane. These results are in good agreement with the XRD results. After annealing at 550 °C two observations can be made. First, the two new peaks (the #1 and #2 peaks) vanished while the peak of the (002) reflections appears at $2\theta = 14.4^\circ$ with a calculated $d = 0.6$ nm. Second, regarding the (100) and (103) reflections, the relative peak intensity increases and the peak width becomes narrow. This indicates the dissociation of the intercalated atoms from the MoS_2 interlayer and restacking of the MoS_2 layers. MoS_2-H_2O demonstrates the similar XRD profile as MoS_2-PEG. However, the #1 and #2 peaks are at $2\theta = 9.0^\circ$ and $2\theta = 18.0^\circ$, respectively, demonstrating a "red-shift" behavior to high angles compared to those of MoS_2-PEG. In addition, the ratios of the peak intensity for $I_{\#1}/I_{(100)}$ and $I_{\#2}/I_{(100)}$ are 2.43 and 0.91 for MoS_2-H_2O, which are obviously lower than the values of 3.74 and 1.02 for MoS_2-PEG. Therefore, MoS_2-PEG achieves larger (00*l*) interlayer spacing and probably a thinner nanosheet than MoS_2-H_2O. Such a microstructure is favorable for the intercalation of Li ions and can alleviate the volume expansion for LIBs during cycling.

The SEM images for MoS_2-H_2O and MoS_2-PEG before and after annealing are displayed in Fig. 3. The low magnification images clearly illustrate the different MoS_2 morphologies. The sample using H_2O (Fig. 3a) as solvent is dominated with agglomerated particles with large dimensions, while that using PEG (Fig. 3c) as solvent is dominated with spherical shapes of diameters about 2 μm. Compared these two samples at high magnification, the latter is more porous than the former, which is favorable for permeation of electrolyte, though the structures of these two samples are both composed by nanosheets. The dimension has not significantly changed after annealing, but lots of extra particles are observed under high magnification (Fig. 3f). These particles show irregular shapes with a size of 1–2 μm. This may be the reason why the XRD peaks regarding the (100) and (103) reflections become sharp and narrow.

Fig. 4 schematically illustrates the formation of the severe lattice distorted spherical MoS_2 nanosheets. During the process of hydrothermal reaction, Mo (VI) in MoO_4^{2-} was reduced by H_2S generated from the hydrolysis of thiourea and forms MoS_2 nanosheets [29,30]. The chemical reaction formula is displayed in Fig. 4. PEG chains contain a large amount of active –O– when dispersed in water, leading to a strong interaction between PEG chains and the metallic ions [20]. PEG thus plays a key role as surfactant to absorb on MoS_2 surface to anchor the spherical morphology. On the other hand, the strong binding force between the active oxygen atoms and the metallic ions may: 1) facilitate the incorporation of PEG chains into the MoS_2 interlayer during forming the MoS_2 nanosheets; and 2) prevent the removal of these intercalated PEG chains from the MoS_2 interlayer when MoS_2-PEG was washed with distilled water, alcohol, and acetone for several times. The residual PEG chains and/or oxygen atoms inherited from the molybdate precursor may contribute to the severe lattice distortion as confirmed by the XRD and TEM characterization.

MoS_2 interlayers can be intercalated by atoms, ions, and polymers. Various characterization methods have been carried out to find out what the intercalated substance is. The FTIR spectra of MoS_2-PEG before and after annealing, MoS_2-H_2O, and PEG400 are compared in Fig. 5a. The vertical dotted lines are a guide for the eye. The two highest peaks for MoS_2-PEG and MoS_2-H_2O are at the same positions of 3430 and 1630 cm^{-1}, which are slightly shifted in contrast to those for PEG400 at 3375 (O–H stretching) and 1645 cm^{-1} (H–O–H deformation), respectively. This indicates that the hydroxyl group is not originated from PEG but from the existence of the surface water, in accordance with the previous result [31]. Compared with MoS_2-H_2O, the additional FTIR peaks for

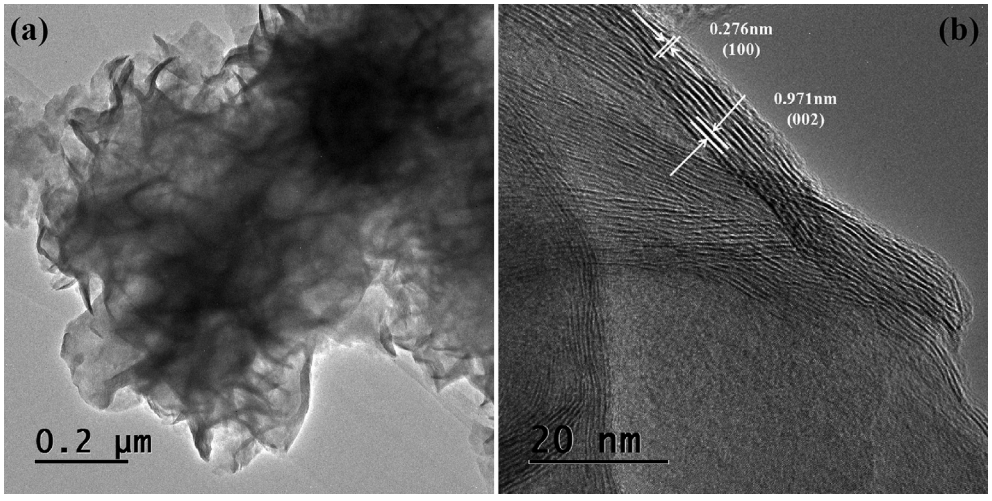

Fig. 2. TEM images for (a) a MoS_2-PEG "flower" and (b) its magnification to see the "petal" containing a few MoS_2 layers.

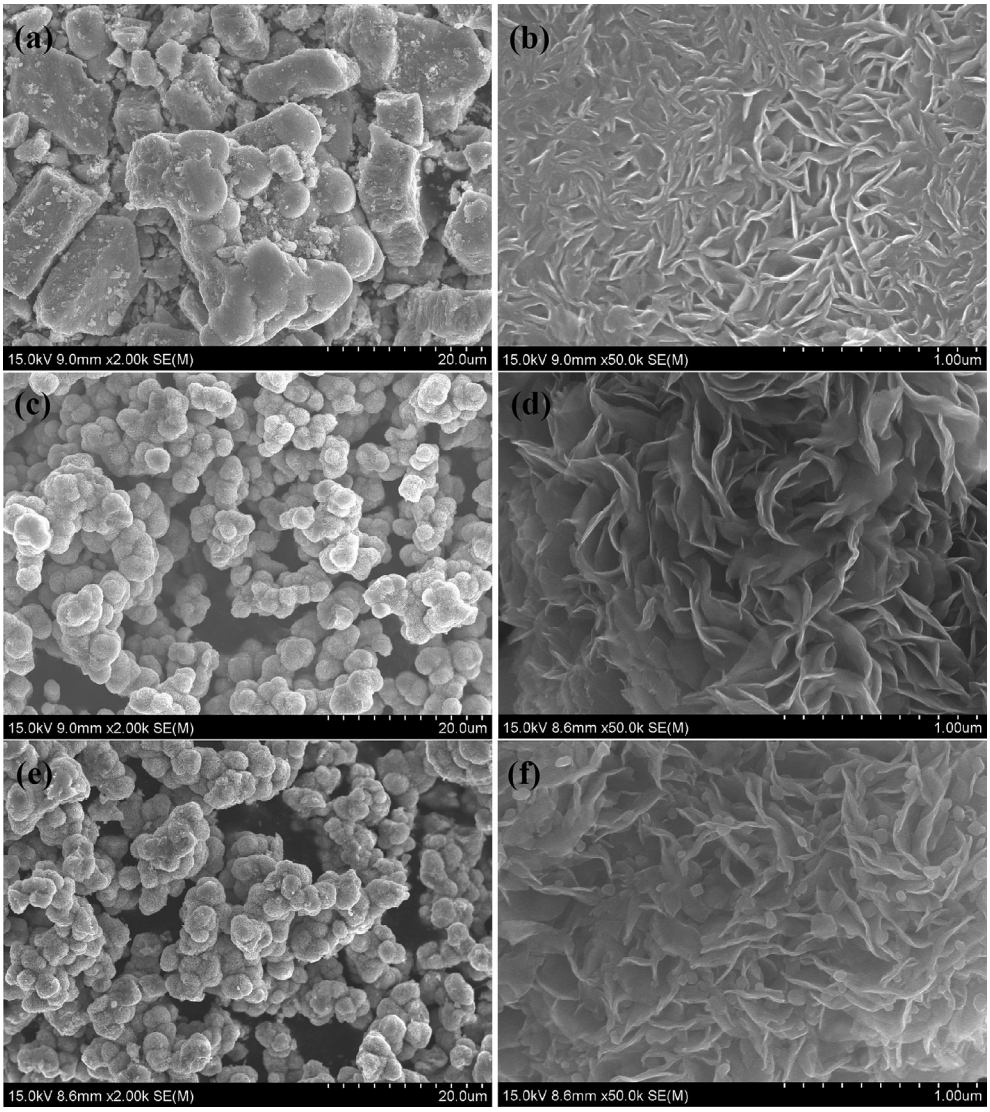

Fig. 3. SEM images with low and high magnifications for MoS_2-H_2O (a,b), MoS_2-PEG (c,d), and MoS_2-PEG-A (e,f).

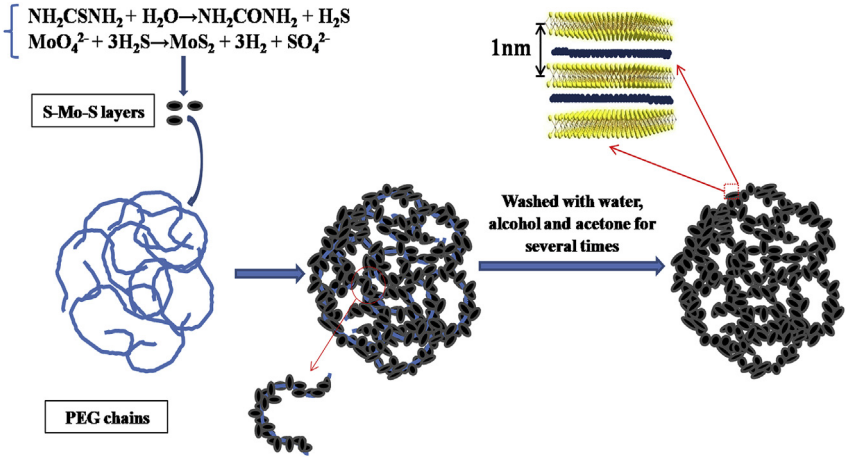

Fig. 4. Schematic representations of the formation of severe lattice distorted spherical MoS_2 nanosheets.

MoS_2-PEG at 1593, 1460, 1260, and 858 cm^{-1} may be ascribed to the PEG chains and/or the oxygen-containing groups inserted into the S-Mo-S interlayers [25,31]. After annealing at 550 °C (MoS_2-PEG-A), most of the FTIR peaks vanished except those at 1624 cm^{-1} and

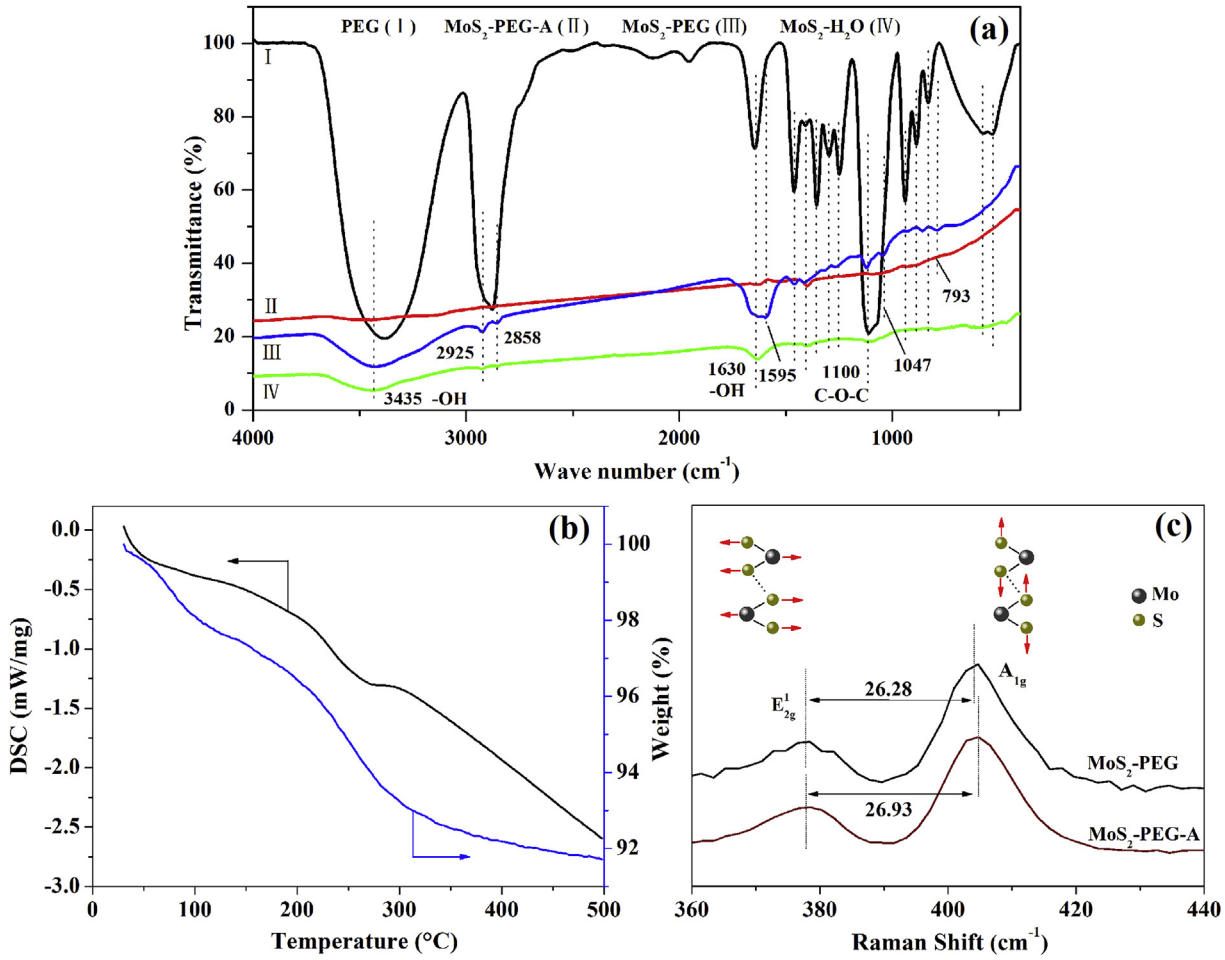

Fig. 5. (a) FTIR spectra of MoS_2-PEG before and after annealing, MoS_2-H_2O, and PEG400 for comparison. (b) DSC/TG curves of MoS_2-PEG. (c) Raman spectra of MoS_2-PEG before and after annealing.

1395 cm^{-1}, and a broad peak from 1126 to 950 cm^{-1}, though the intensities of these remaining peaks are significantly suppressed in contrast to those before annealing. Since these remaining peaks also appear in MoS_2-H_2O, they may come from the molybdate and thiourea precursors. Although the samples were washed for several times, the weak characteristic peaks of PEG400 can still be observed from MoS_2-PEG, indicating a slight incorporation of PEG or its related functional groups in the final product. The DSC/TG curves for MoS_2-PEG (Fig. 5b) illustrate two endothermic peaks at about 90 °C and 300 °C. Based on the FTIR results and the results previously reported [31], we believe that the former is related to the evaporation of the adsorbate such as the surface water and the latter may be induced by dissociation/decomposition of the intercalated PEG.

The EDS measurements (Table 1) also show that after annealing the amount of C and O decrease from 16.10 wt% and 7.49 wt% to 10.24 wt% and 2.71 wt%, respectively. On the other hand, the atomic ratio of Mo:S after annealing changes from 1:2.35 to 1:1.96, indicating a variation from a S-rich composition to a nearly stoichiometric composition. High degree of unsaturated sulfur atoms for MoS_2-PEG further confirms a severe distorted structure [28,32].

The Raman spectra of MoS_2 before and after annealing are shown in Fig. 5c. For both samples, two typical stretching modes of MoS_2 are observed corresponding to the out-of-plane A_{1g} mode and the in-plane E^1_{2g} mode, which can be ascribed to the vibration of S atoms in the opposite direction along *c*-axis and an opposite vibration of the Mo atom with respect to two S atoms perpendicular to *c*-axis [33], respectively. After annealing, the A_{1g} vibration stiffens with a blue shift from 403.93 cm^{-1}–404.68 cm^{-1} while the E^1_{2g} vibration shows a negligible red shift from 377.65 cm^{-1}–377.75 cm^{-1}. This behavior is in agreement with that for few-layer MoS_2 that restacking has a weak perturbation on the in-plane E^1_{2g} vibration [33], but partially different from that for a single-layer MoS_2 [34]. Revealed by that paper [34], when a single-layer MoS_2 restacks to form bulk MoS_2, the interlayer van der Waals force not only enhances the out-of-plane A_{1g} vibration but also softens the E^1_{2g} vibration. Additionally, the difference of the Raman frequencies between the A_{1g} and E^1_{2g} modes (Δ) is regarded as an indicator of the layer thickness for MoS_2 [34]. After annealing, the difference of the two modes for MoS_2-PEG expands from $\Delta = 26.28\ cm^{-1}$ to $\Delta = 26.93\ cm^{-1}$, indicating an increased thickness of the nanosheets after annealing. In view of these results of Raman spectra, MoS_2-PEG is composed by the ultrathin MoS_2 nanosheets with only few layers, in line with the observation from

Table 1
Elemental Analyses of MoS_2 before and after annealing.

	wt%				atomic ratio normalized to Mo			
	Mo	S	O	C	Mo	S	O	C
MoS_2-PEG	42.83	33.58	7.49	16.1	1	2.35	1.05	3.00
MoS_2-PEG-A	52.5	34.56	2.71	10.24	1	1.96	0.31	1.56

TEM (Fig. 2b). When the samples subjected to high temperature heat treatment, the layer becomes thicker because of the dissociation of the intercalated atoms.

Since the MoS_2 nanosheets contain only a few S–Mo–S layers, XPS is very suitable for evaluating their interfacial nature and chemical species. Fig. 6a compares the XPS spectra for MoS_2-PEG before and after annealing. Both samples are composed of Mo, S, O and C elements. However, the relative intensities of O and C after annealing are significantly reduced while those of Mo and S are by contrast increased, indicating removal of C and O with heat treatment. The high-resolution XPS peaks of Mo 3d (Fig. 6b) show two doublet bands assigned to Mo $3d_{3/2}$ and Mo $3d_{5/2}$. These two peaks for the samples before and after annealing are obviously different. The spectrum of MoS_2-PEG can be deconvoluted into four peaks belonging to the 1T and 2H phases of MoS_2 [27,35], indicating a mixture structural type of MoS_2-PEG. The quantitative analysis of

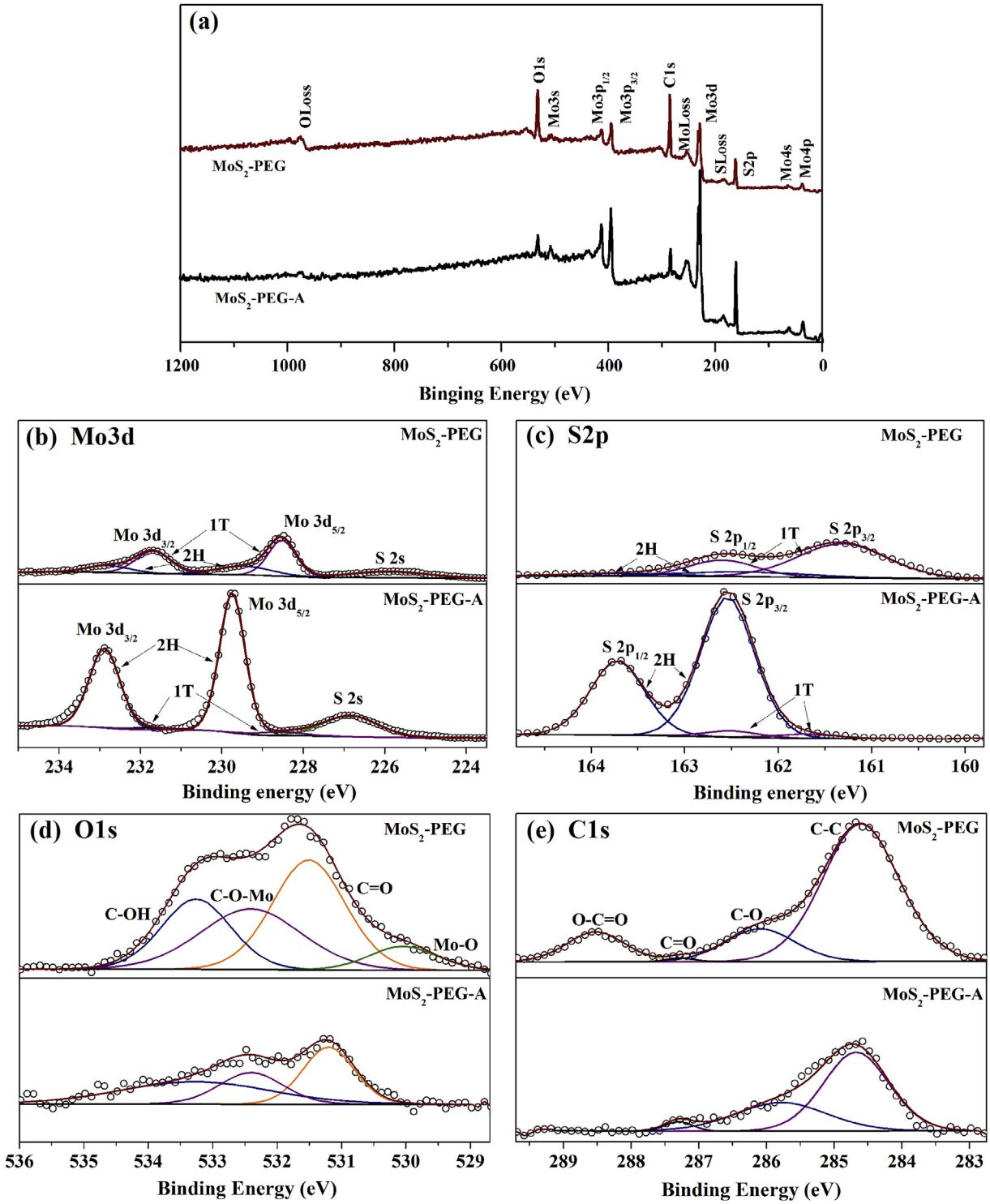

Fig. 6. XPS spectra of MoS_2-PEG and MoS_2-PEG-A. (a) Survey spectra, and high resolution XPS spectra of Mo3d (b), S2p (b), O1s (c), and C1s (d).

Table 2
Binding energy (BE) and elemental analysis of Mo 3d and S 2p for MoS_2-PEG and MoS_2-PEG-A.

			MoS_2-PEG		MoS_2-PEG-A	
			BE (eV)	at%	BE (eV)	at%
Mo	1T	$3d_{3/2}$	231.69	30.35	231.59	2.82
		$3d_{5/2}$	228.53	38.91	228.53	1.69
	2H	$3d_{3/2}$	232.81	12.06	232.88	38.98
		$3d_{5/2}$	229.46	18.68	229.75	56.50
S	1T	$2p_{3/2}$	161.31	59.88	161.7	1.88
		$2p_{1/2}$	162.60	21.89	162.5	2.26
	2H	$2p_{3/2}$	162.38	12.57	162.54	62.5
		$2p_{1/2}$	163.69	5.39	163.72	33.13

the 1T and 2H phases can be obtained by curve fitting. The results are listed in Table 2. MoS_2-PEG is composed by 69 at% of the 1T phase and 31 at% of the 2H phase. The metallic 1T phase is favorable for both higher electrical conductivity and faster ion motility compared to the semiconducting 2H phase [7,8]. However, the 1T phase almost fully converts to the 2H phase after annealing as MoS_2-PEG-A is composed by 96 at% of the 2H phase and only 4 at% of the 1T phase. The high-resolution XPS peaks of S 2p (Fig. 6c), assigned to $2p_{1/2}$ and $2p_{3/2}$, show the similar changes before and after annealing as those of Mo3d.

The XPS survey spectra of O 1s and C 1s for the samples before and after annealing are also different, as illustrated in Fig. 6d–e. Deconvolution of the complicated O 1s region of MoS_2-PEG indicates the existence of C=O, Mo–O–C, C–OH, and Mo–O bonds [25,36]. On the other hand, deconvolution of the C 1s region indicates the existence of C–C, C–O, C=O, and O–C=O bonds [25]. This further confirms that the expanded interlayer spacing of MoS_2-PEG is induced by intercalation of the C and O atoms. By contrast, the peaks for Mo–O and O–C=O bonds disappear and the relative intensities of the other peaks decrease after annealing. These results are in good agreement with the FTIR, EDS, and Raman results above mentioned, confirming the partial removal of C and O after heat treatment. Metal-oxygen bonds were found to play an important role to enhance the electron transport in the results previously reported [37,38]. The theoretical study reveals a strong oxygen bridge in C–O–Ni linkage, which contains a large electron charge overlap providing a short diffusion pathway for lithium ions and electrons among the sheet-like structure [38]. Therefore, the covalent Mo–O–C (and Mo–O) bonding between the S-Mo-S layers is favorable for the structural stability and the rate capability, thus a good electrochemical performance for MoS_2-PEG is anticipated.

3.2. Electrochemical performances

Fig. 7a shows the cyclic voltammogram (CV) curves of MoS_2-PEG during the first four cycles at 0.2 mV s^{-1} in the voltage range of 0.01–3 V. In the first cathodic scan, there appears a broadened reduction peak at 1.5 V and a sharp reduction peak at 0.41 V. The peak at 1.5 V corresponds to the intercalation of Li ions into MoS_2

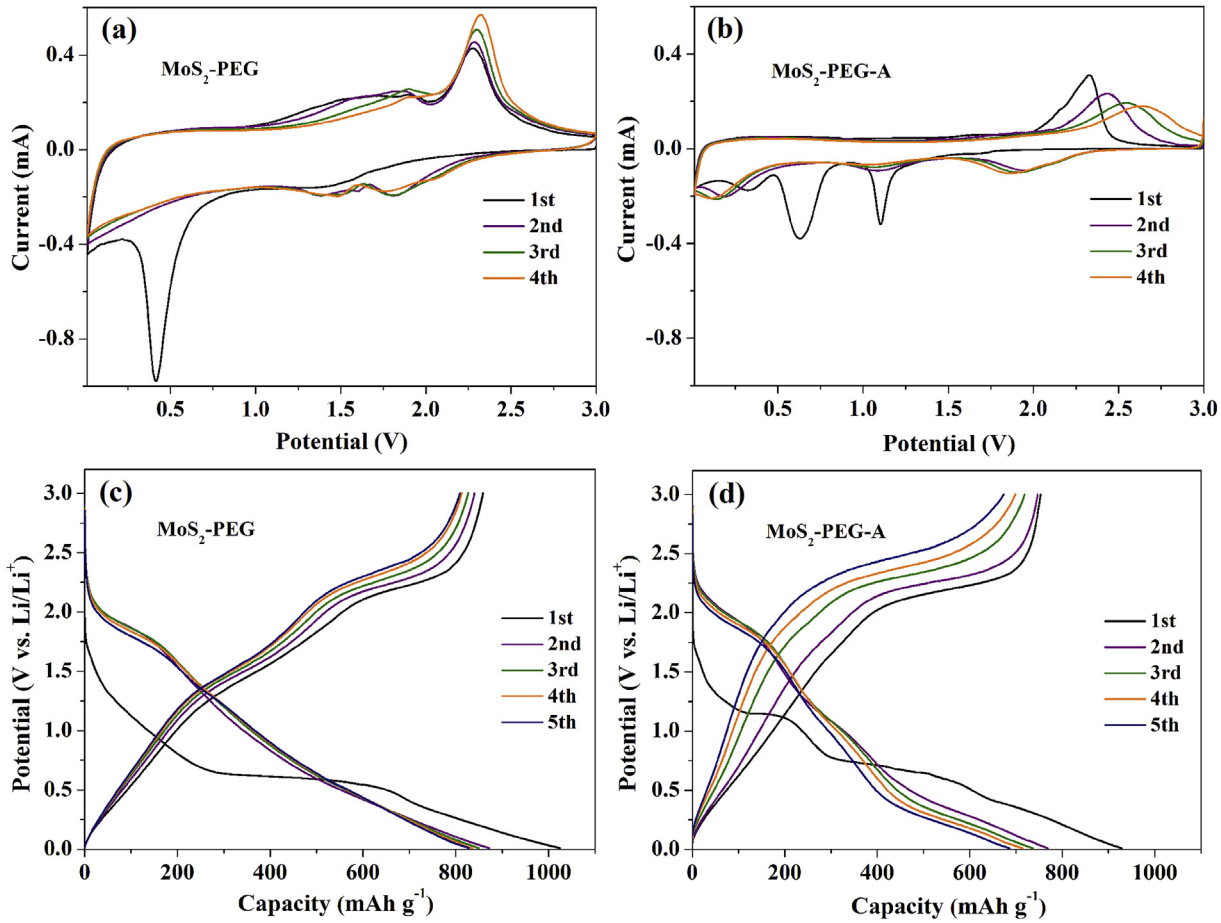

Fig. 7. Cyclic voltammograms of MoS_2-PEG (a) and MoS_2-PEG-A (b) at a scan rate of 0.1 mV s^{-1}. The charging-discharging curves of MoS_2-PEG (c) and MoS_2-PEG-A (d) at a current density of 0.1 A g^{-1}.

layers to form Li_xMoS_2, which normally appears at 1.0 V for MoS_2 with unexpanded interlayer spacing. This variation is originated from the different electronic environment and different sites or quantity of defects in the MoS_2 due to its interlayer expanded by intercalation of foreign atoms [39–41]. The peak at 0.41 V may be attributed to the conversion of Li_xMoS_2 to metallic Mo and Li_2S. In the following anodic scan, there appears two oxidation peaks at about 1.7 V and 2.3 V, which are associated to the oxidation of Mo to MoS_2 because of the inhomogeneous delithiation induced by the defect sites and the formation of MoS_2, respectively [42]. In the second cathodic scan, the peaks at 0.41 V and 1.5 V disappeared, and there appears another two peaks at about 1.8 V and 1.37 V, which are attributed to the conversion reaction of S to Li_2S and the association of Li and Mo, respectively [28]. In contrast, MoS_2-PEG-A shows a different CV profile, as displayed in Fig. 7b. The peak regarding formation of Li_xMoS_2 appears at 1.1 V instead of at 1.5 V for MoS_2-PEG, indicating a higher crystal structure and a lower quantity of defects. This is also confirmed by the following anodic scan with a missing peak at 1.7 V compared to MoS_2-PEG. Moreover, the oxidation peak shown in MoS_2-PEG-A more obviously shifts to a higher voltage in contrast to that shown in MoS_2-PEG, indicating a larger polarization. This polarization can also be observed from the discharge/charge curves shown in Fig. 7d.

Fig. 7c and d respectively show the first five discharge/charge curves for MoS_2-PEG and MoS_2-PEG-A at a current density of 100 mA g^{-1} from 0.01 to 3 V. The potential plateaus shown in both of the cells are in accordance with the CV results. The initial discharge capacities for MoS_2-PEG and MoS_2-PEG-A are 1082.5 and 928.5 mAh g^{-1}, respectively. The irreversible capacity-losses between the first discharge and charge process for these two cells are 20% and 19%, respectively, which is mainly due to the formation of SEI film by the decomposition of the electrolyte and the Li incorporation into SEI. Additionally, MoS_2-PEG demonstrates a better reversibility than MoS_2-PEG-A. Therefore, comparing MoS_2-PEG with MoS_2-PEG-A and considering the recovered distortion and a reduced defect concentration after annealing, one can conclude that distortion/defects are beneficial to enhance the electrochemical performance but have negligible influence on the irreversible capacity-loss.

The cycling performance and Coulombic efficiency for MoS_2-PEG, MoS_2-H_2O and MoS_2-PEG-A are compared between 0.01 and 3 V at a current rate of 0.2 A g^{-1}, as shown in Fig. 8a. The initial capacities for these specimens are comparable with the values of 1038.2, 972.0, and 1028.5 mAh g^{-1}, respectively. Although the initial Coulombic efficiency is only 78% due to the formation of SEI film by the decomposition of the electrolyte and Li incorporation into SEI, the specimens show excellent reversibility with a Coulombic efficiency approaching 100% after the second cycle, indicating a facile insertion/extraction of Li ion process [43]. All three compounds exhibit a capacity climbing after fading for a

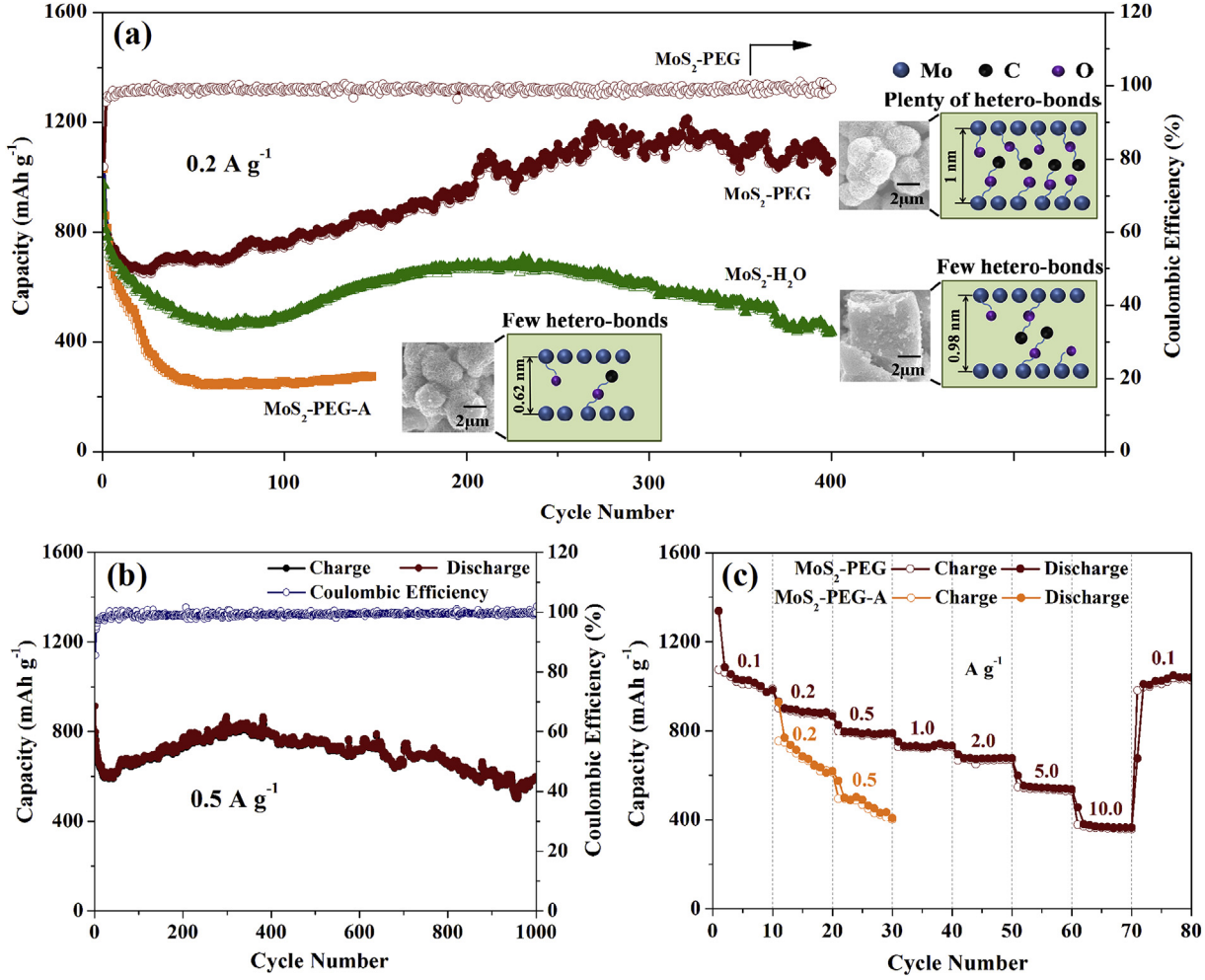

Fig. 8. (a) Cycling performance and Coulombic efficiency of MoS_2-PEG, MoS_2-PEG-A, and MoS_2-H_2O electrodes at a current rate of 0.2 A g^{-1}. (b) Cycling performance and Coulombic efficiency of MoS_2-PEG at a current rate of 0.5 A g^{-1}. (c) Rate capability of MoS_2-PEG and MoS_2-PEG-A.

number of cycles. The continuous capacity increase can be attributed to several points including: (1) interlayer expansion and electrochemical delamination of the layered nanostructure after several cycles [25,42,44–46] and, (2) the formation of electrochemical active sites after cycling due to gradual extension of the defects/vacancies [42]. EIS measurements were performed after 400 cycles, as shown in Figure S1 and Table S1 in Supplementary Information. Compared the capacitance C_2 before cycling, the value is one order of magnitude higher after 400 cycles, indicating an increase of electrochemical surface area on the electrode. This capacity climbing effect may be mitigated by incorporating buffer layer such as graphene or carbon nanotube. Among these three specimens, MoS_2-PEG demonstrates the best cycling performance and the highest capacity up to 1200 mAh g^{-1}. Compared with MoS_2-PEG-A, MoS_2-PEG contains expanded interlayer spacing as well as a plenty of Mo–O–C (and Mo–O) hetero-bonds and defects. On the other hand, compared with MoS_2-H_2O composed of agglomerated bulk, MoS_2-PEG is composed of "flowers" with small particle sizes (~2 μm). Therefore, both expanded interlayer spacing and Mo–O–C (and Mo–O) hetero-bonds make great contributions to the excellent cycling performance and the high capacity. The advantages including expanded interlayer spacing, hetero-bonds, and flower-like morphology ensure MoS_2-PEG possessing the superior ability for buffering the mechanical stress and the huge volume change during Li^+ insertion and extraction [39]. Our future work is to increase the amount of the hetero-bonds and defects in MoS_2 and to investigate their status after cycling by using Raman and/or XPS. Prolonged cycling tests (Fig. 8b) were performed on MoS_2-PEG at a current rate of 0.5 A g^{-1}. The discharge capacity still maintains at over 600 mAh g^{-1} after 1000 cycles with a Coulombic efficiency of 99.9%. The discharge capacity values of MoS_2-PEG and part of recently reported MoS_2-based anodes with their interlayer distances are summarized in Table 3. Obviously, MoS_2-PEG exhibits a moderate reversible capacity with an excellent cycling stability among MoS_2-based anodes. It is notable that none carbon-related incorporation/decoration is performed on MoS_2-PEG, otherwise a higher reversible capacity and better cycling performance are expected. The final gradual capacity fading can be explained by the microstructural damages (pulverization) induced by volume changes. The SEM and HRTEM images and ex situ XRD profile of the positive electrode after 800 cycles are shown in Figure S2 and S3 in Supplementary Information. The SEM images show that the flower-like MoS_2 nanosheets were partially pulverized and became thicker after cycling in contrast to the pristine electrode. Both the HRTEM image and the ex situ XRD result reveal that the pristine MoS_2 nanosheets disappear while amorphous phase and nanocrystalline appear after cycling, which cause the capacity decay.

In addition to the cycling stability, a good rate capability is important for practical application. Fig. 8c shows the rate capability of MoS_2-PEG electrode compared with MoS_2-PEG-A. The reversible capacity is about 982 mAh g^{-1} at the current density of 0.1 A g^{-1}. The reversible capacities of MoS_2-PEG maintain at 866, 790, 733, 676, 537, and 364 mAh g^{-1} at current densities of 0.2, 0.5, 1.0, 2.0, 5.0 and 10.0 A g^{-1}, respectively. When the current density turns back from 10 to 0.1 A g^{-1}, the discharge capacity recovers to 1010 mAh g^{-1}, indicating a high cycle stability. By contrast, the capacity of MoS_2-PEG-A shows a fast capacity fading with increasing current density. The capacity rapidly decays from 768 to 499 mAh g^{-1} as current density increases from 0.2 to 0.5 A g^{-1}. The superior rate capability of MoS_2-PEG over MoS_2-PEG-A is attributed to the enlarged interlayer spacing favorable to lithiation/delithiation [47]. Coupling of the Mo–O–C (and Mo–O) hetero-bonds facilitates an effective electron transfer path between the S-Mo-S layers as well as enhances the structural stability [25,48], and the 1T-like behavior is favorable to enhance lithium storage capability and rate capability [49,50]. Although 1T-like MoS_2 is reconstructed to the other nano phases after cycling, the initial 1T-like structure is previously reported to provide a special structure with expanded interlayer spacing as well as a high concentration of active sites to achieve prominent electrochemical properties [49,50]. The comparison of the electrodes cut from the center with that cut from the edge is shown in Figure S4. The former shows a rapid capacity fading until stabilizing at a low capacity, either for the cycling tests or for the rate capability test. However, the electrode cut from the edge part demonstrates a stable shoulder before 35 cycles and after that decreases to the same specific capacity as those cut from the center part. The thickness and the loading mass of the electrodes significantly affect the behavior of electrochemical performance. Figure S5 shows the galvanostatic charge-discharge properties of $LiFePO_4$/MoS_2-PEG full-cells. The initial charge and discharge capacities are 1290.0 and 948.7 mAh g^{-1}, respectively, in good agreement with the values based on MoS_2-PEG half-cells. The discharge specific capacity maintains at 920.6 mAh g^{-1} with a coulombic efficiency of 97.1% in the following several cycles, indicating good electrochemical performance of the MoS2-PEG anode in full-cells.

EIS measurements were performed to further understand the rate capability difference for MoS_2-PEG before and after annealing. The Nyquist plots of the impedance at room temperature for MoS_2-

Table 3
The discharge capacities of MoS_2-PEG compared with recently reported MoS_2-based anode materials in lithium ion batteries.

MoS_2 type	Interlayer spacing (nm)	Discharge capacity (mAh g^{-1})	Current density (A g^{-1})	Cycles
MoS_2-PEG (TW)	0.97	1150	0.2	400
		600	0.5	1000
MoO_2@MoS_2 [48]	0.62	1016	0.1	200
MoS_2-46.8%/SRGO [53]	0.629	724.2	0.05	200
Fe_3O_4/$Fe_{1-x}S$@C@MoS_2 [54]	0.63	1003	0.2	100
Tremella-like MoS_2 [55]	0.647	693	0.039	50
MoS_2@f-graphene [56]	0.652	1064	0.1	100
GODs/MoS_2 [57]	0.78–0.80	1031	0.1	80
MoS_2-AC-RGO-0.1 [58]	0.98	910	0.2	120
MoS_2/G [37]	0.63	1077	0.1	150
N-C@MoS_2 [59]	0.65	1050	0.15	300
MoS_2/Ti_3C_4-MXene@C [60]	0.64	1130	1.0	700
MoS_2/PANI [61]	1.08	1207	0.2	100
Bubble MoS_2-C [46]	0.62	1500–2000	0.5	600

TW: This work, without any carbon-related decoration/incorporation.

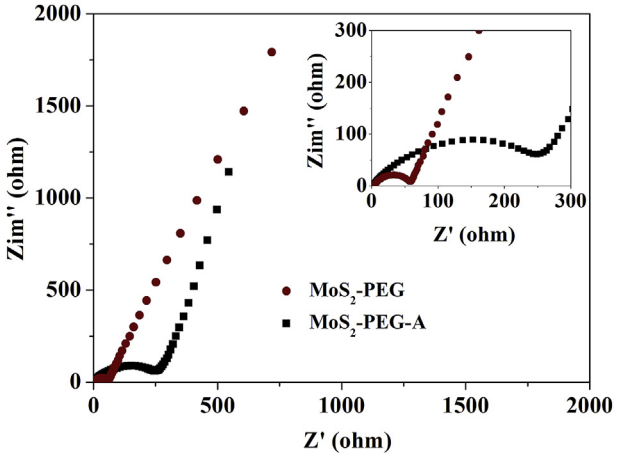

Fig. 9. Nyquist plots of MoS_2-PEG and MoS_2-PEG-A. The insert magnifies the Nyquist plots at high and medium frequency regions.

PEG and MoS_2-PEG-A are shown in Fig. 9. The impedance spectrum can be separated into an intercept of the Z′ axis at high frequency region, a high and a medium frequency semicircle, and a long tail at low frequency region. These parts from high to low frequencies are ascribed to the bulk resistance, the resistance of SEI film, the charge transfer resistance on the electrode/electrolyte interface, and the Warburg impedance related to the Li^+ diffusion in the electrode materials [51,52]. The semicircle of MoS_2-PEG is significantly smaller than that of MoS_2-PEG-A, indicating a higher conductivity of the former attributed to its 1T-like metallic behavior and the special structure (expanded interlayer spacing, hetero-bonds, and extended active sites). The high conductivity of MoS_2-PEG is beneficial to enhance charge transfer kinetics.

4. Conclusions

In summary, a facile synthesis approach toward severe lattice distorted MoS_2 nanosheets was discovered by a PEG-assisted hydrothermal synthesis. Compared with pure water as solvent, the PEG400 addictive not only acts as surfactant to form flower-like morphology, but, more importantly, also modifies the microstructure of MoS_2, which enlarges the interlayer spacing and reduces nanosheet layers, and thus giving rise to a 1T-like metallic behavior with a high conductivity. Furthermore, the incorporation of oxygen- and carbon-containing groups into MoS_2 interlayers leads to the coupling of Mo—O—C (and Mo—O) hetero-bonds, which facilitates the electron transport rate and the structural stability of MoS_2. This special structure enables MoS_2 to achieve superior electrochemical performance, independent of carbon coating/supporting. Prepared via a PEG-assisted synthesis route, MoS_2 maintains the reversible capacity up to 1200 (600) mAh g^{-1} over 400 (1000) cycles at a current density of 0.2 (0.5) A g^{-1} and 364 mAh g^{-1} at a current density of 10 A g^{-1}. Future work is to further enhance the electrochemical performance of MoS_2-PEG through a carbon-related incorporation/decoration.

Acknowledgments

This work was supported by the National Science Foundation of China (51525205), and the Foundation of Higher Education of Hebei (ZD2016033).

Appendix A. Supplementary data

Supplementary data related to this article can be found at https://doi.org/10.1016/j.electacta.2018.01.023.

References

[1] Y. Yao, N. Xu, D. Guan, J. Li, Z. Zhuang, L. Zhou, C. Shi, X. Liu, L. Mai, Facet-selective deposition of FeOx on alpha-MoO_3 nanobelts for lithium storage, ACS Appl. Mater. Interfaces 9 (2017) 39425–39431.
[2] L. Zhou, Z. Zhuang, H. Zhao, M. Lin, D. Zhao, L. Mai, Intricate hollow structures: controlled synthesis and applications in energy storage and conversion, Adv. Mater. 29 (2017) 1602914.
[3] K.A. Owusu, L. Qu, J. Li, Z. Wang, K. Zhao, C. Yang, K.M. Hercule, C. Lin, C. Shi, Q. Wei, L. Zhou, L. Mai, Low-crystalline iron oxide hydroxide nanoparticle anode for high-performance supercapacitors, Nat. Commun. 8 (2017) 14264.
[4] E.S. Pampal, E. Stojanovska, B. Simon, A. Kilic, A review of nanofibrous structures in lithium ion batteries, J. Power Sources 300 (2015) 199–215.
[5] X.L. Wu, Y.G. Guo, L.J. Wan, Rational design of anode materials based on Group IVA elements (Si, Ge, and Sn) for lithium-ion batteries, Chem. Asian J. 8 (2013) 1948–1958.
[6] X. Chia, A.Y. Eng, A. Ambrosi, S.M. Tan, M. Pumera, Electrochemistry of nanostructured layered transition-metal dichalcogenides, Chem. Rev. 115 (2015) 11941–11966.
[7] X. Cao, C. Tan, X. Zhang, W. Zhao, H. Zhang, Solution-processed two-dimensional metal dichalcogenide-based nanomaterials for energy storage and conversion, Adv. Mater. 28 (2016) 6167–6196.
[8] X. Hu, W. Zhang, X. Liu, Y. Mei, Y. Huang, Nanostructured Mo-based electrode materials for electrochemical energy storage, Chem. Soc. Rev. 44 (2015) 2376–2404.
[9] X. Wang, W. Xing, X. Feng, L. Song, Y. Hu, MoS_2/Polymer nanocomposites: preparation, properties, and applications, Polym. Rev. 57 (2017) 440–466.
[10] L. Huang, Q. Wei, X. Xu, C. Shi, X. Liu, L. Zhou, L. Mai, Methyl-functionalized MoS_2 nanosheets with reduced lattice breathing for enhanced pseudocapacitive sodium storage, Phys. Chem. Chem. Phys. 19 (2017) 13696–13702.
[11] Y. Yan, B. Xia, Z. Xu, X. Wang, Recent development of molybdenum sulfides as advanced electrocatalysts for hydrogen evolution reaction, ACS Catal. 4 (2014) 1693–1705.
[12] M.Q. Wen, T. Xiong, Z.G. Zang, W. Wei, X.S. Tang, F. Dong, Synthesis of MoS_2/g-C_3N_4 nanocomposites with enhanced visible-light photocatalytic activity for the removal of nitric oxide (NO), Optic Express 24 (2016) 10205–10212.
[13] X. Zhou, L.J. Wan, Y.G. Guo, Facile synthesis of MoS_2@CMK-3 nanocomposite as an improved anode material for lithium-ion batteries, Nanoscale 4 (2012) 5868–5871.
[14] X. Wang, Q. Weng, Y. Yang, Y. Bando, D. Golberg, Hybrid two-dimensional materials in rechargeable battery applications and their microscopic mechanisms, Chem. Soc. Rev. 45 (2016) 4042–4073.
[15] G. Chen, L. Yan, H. Luo, S. Guo, Nanoscale engineering of heterostructured anode materials for boosting lithium-ion storage, Adv. Mater. 28 (2016) 7580–7602.
[16] A. Sajedi-Moghaddam, E. Saievar-Iranizad, M. Pumera, Two-dimensional transition metal dichalcogenide/conducting polymer composites: synthesis and applications, Nanoscale 9 (2017) 8052–8065.
[17] X.-Y. Yu, L. Yu, X.W.D. Lou, Metal sulfide hollow nanostructures for electrochemical energy storage, Adv. Energy Mater. 6 (2016) 1501333.
[18] K.D. Rasamani, F. Alimohammadi, Y. Sun, Interlayer-expanded MoS_2, Mater. Today 20 (2017) 83–91.
[19] X.L. Gou, F.Y. Cheng, Y.H. Shi, L. Zhang, S.J. Peng, J. Chen, P.W. Shen, Shape-controlled synthesis of ternary chalcogenide $ZnIn_2S_4$ and $CuIn(S,Se)_2$ nano-/microstructures via facile solution route, J. Am. Chem. Soc. 128 (2006) 7222–7229.
[20] X. Shi, L. Pan, S. Chen, Y. Xiao, Q. Liu, L. Yuan, J. Sun, L. Cai, Zn(II)-PEG 300 globules as soft template for the synthesis of hexagonal ZnO micronuts by the hydrothermal reaction method, Langmuir 25 (2009) 5940–5948.
[21] Z. Wu, D. Wang, A. Sun, Surfactant-assisted fabrication of MoS_2 nanospheres, J. Mater. Sci. 45 (2010) 182–187.
[22] W. Liu, S. He, Y. Wang, Y. Dou, D. Pan, Y. Feng, G. Qian, J. Xu, S. Miao, PEG-assisted synthesis of homogeneous carbon nanotubes-MoS_2-carbon as a counter electrode for dye-sensitized solar cells, Electrochim. Acta 144 (2014) 119–126.
[23] T. Liu, C. Wang, X. Gu, H. Gong, L. Cheng, X. Shi, L. Feng, B. Sun, Z. Liu, Drug delivery with PEGylated MoS_2 nano-sheets for combined photothermal and chemotherapy of cancer, Adv. Mater. 26 (2014) 3433–3440.
[24] T.Z. Zou, J.P. Tu, H.D. Huang, D.M. Lai, L.L. Zhang, D.N. He, Preparation and tribological properties of inorganic fullerene-like MoS_2, Adv. Eng. Mater. 8 (2006) 289–293.
[25] Y. Teng, H. Zhao, Z. Zhang, Z. Li, Q. Xia, Y. Zhang, L. Zhao, X. Du, Z. Du, P. Lv, K. Swierczek, MoS_2 nanosheets vertically grown on graphene sheets for lithium-ion battery anodes, ACS Nano 10 (2016) 8526–8535.
[26] M.R. Gao, M.K. Chan, Y. Sun, ge-terminated molybdenum disulfide with a 9.4-A interlayer spacing for electrochemical hydrogen production, Nat. Commun. 6 (2015) 7493.
[27] M. Acerce, D. Voiry, M. Chhowalla, Metallic 1T phase MoS_2 nanosheets as supercapacitor electrode materials, Nat. Nanotechnol. 10 (2015) 313–318.
[28] Z. Wu, B. Li, Y. Xue, J. Li, Y. Zhang, F. Gao, Fabrication of defect-rich MoS_2 ultrathin nanosheets for application in lithium-ion batteries and supercapacitors, J. Mater. Chem. 3 (2015) 19445–19454.
[29] S. Wang, G. Li, G. Du, X. Jiang, C. Feng, Z. Guo, S.-J. Kim, Hydrothermal synthesis of molybdenum disulfide for lithium ion battery applications, Chin. J. Chem. Eng. 18 (2010) 910–913.
[30] J. Wang, J. Liu, J. Luo, P. Liang, D. Chao, L. Lai, J. Lin, Z. Shen, MoS_2 architectures supported on graphene foam/carbon nanotube hybrid films: highly integrated frameworks with ideal contact for superior lithium storage, J. Mater. Chem. 3 (2015) 17534–17543.
[31] D. Wang, X. Zhang, S. Bao, Z. Zhang, H. Fei, Z. Wu, Phase engineering of a multiphasic 1T/2H MoS_2 catalyst for highly efficient hydrogen evolution, J. Mater. Chem. 5 (2017) 2681–2688.
[32] J. Xie, H. Zhang, S. Li, R. Wang, X. Sun, M. Zhou, J. Zhou, X.W. Lou, Y. Xie, Defect-rich MoS_2 ultrathin nanosheets with additional active edge sites for enhanced electrocatalytic hydrogen evolution, Adv. Mater. 25 (2013) 5807–5813.
[33] S. Zhang, B.V.R. Chowdari, Z. Wen, J. Jin, J. Yang, Constructing highly oriented configuration by few-layer MoS_2: toward high-performance lithium-ion batteries and hydrogen evolution reactions, ACS Nano 9 (2015) 12464–12472.
[34] C. Lee, H. Yan, L.E. Brus, T.F. Heinz, J. Hone, S. Ryu, Anomalous lattice vibrations of single- and few-layer MoS_2, ACS Nano 4 (2010) 2695–2700.
[35] Z. Chen, K. Leng, X. Zhao, S. Malkhandi, W. Tang, B. Tian, L. Dong, L. Zheng, M. Lin, B.S. Yeo, K.P. Loh, Interface confined hydrogen evolution reaction in zero valent metal nanoparticles-intercalated molybdenum disulfide, Nat. Commun. 8 (2017) 14548.
[36] J. Xie, J. Zhang, S. Li, F. Grote, X. Zhang, H. Zhang, R. Wang, Y. Lei, B. Pan, Y. Xie, Controllable disorder engineering in oxygen-incorporated MoS_2 ultrathin nanosheets for efficient hydrogen evolution, J. Am. Chem. Soc. 135 (2013)

17881–17888.
[37] Y. Teng, H. Zhao, Z. Zhang, Z. Li, Q. Xia, Y. Zhang, L. Zhao, X. Du, Z. Du, P. Lv, K. Swierczek, MoS_2 nanosheets vertically grown on graphene sheets for lithium-ion battery anodes, ACS Nano 10 (2016) 8526–8535.
[38] G.M. Zhou, D.W. Wang, L.C. Yin, N. Li, F. Li, H.M. Chen, Oxygen bridges between NiO nanosheets and graphene for improvement of lithium storage, ACS Nano 6 (2012) 3214–3223.
[39] Y. Lu, X. Yao, J. Yin, G. Peng, P. Cui, X. Xu, MoS_2 nanoflowers consisting of nanosheets with a controllable interlayer distance as high-performance lithium ion battery anodes, RSC Adv 5 (2015) 7938–7943.
[40] K. Chang, W. Chen, In situ synthesis of MoS_2/graphene nanosheet composites with extraordinarily high electrochemical performance for lithium ion batteries, Chem. Commun. 47 (2011) 4252–4254.
[41] U.K. Sen, S. Mitra, High-rate and high-energy-density lithium-ion battery anode containing 2D MoS_2 nanowall and cellulose binder, ACS Appl. Mater. Interfaces 5 (2013) 1240–1247.
[42] K. Chang, D. Geng, X. Li, J. Yang, Y. Tang, M. Cai, R. Li, X. Sun, Ultrathin MoS_2/nitrogen-doped graphene nanosheets with highly reversible lithium storage, Adv. Energy Mater. 3 (2013) 839–844.
[43] L. Zhang, L. Lu, D. Zhang, W. Hu, N. Wang, B. Xu, Y. Li, H. Zeng, Dual-buffered SnSe@CNFs as negative electrode with outstanding lithium storage performance, Electrochim. Acta 209 (2016) 423–429.
[44] J. Xu, J. Zhu, X. Yang, S. Cao, J. Yu, M. Shalom, M. Antonietti, Synthesis of organized layered carbon by self-templating of dithiooxamide, Adv. Mater. 28 (2016) 6727–6733.
[45] Y. Zheng, T. Zhou, X. Zhao, W.K. Pang, H. Gao, S. Li, Z. Zhou, H. Liu, Z. Guo, Atomic interface engineering and electric-field effect in ultrathin Bi_2MoO_6 nanosheets for superior lithium ion storage, Adv. Mater. 29 (2017) 1700396.
[46] P. Wang, J. Tian, J. Hu, X. Zhou, C. Li, Supernormal conversion anode consisting of high-density MoS_2 bubbles wrapped in thin carbon network by self-sulfuration of polyoxometalate complex, ACS Nano 11 (2017) 7390–7400.
[47] T.S. Sahu, S. Mitra, Exfoliated MoS_2 sheets and reduced graphene oxide-an excellent and fast anode for sodium-ion battery, Sci. Rep. 5 (2015) 12571.
[48] Z. Xu, T. Wang, L. Kong, K. Yao, H. Fu, K. Li, L. Cao, J. Huang, Q. Zhang, MoO_2@ MoS_2 nanoarchitectures for high-loading advanced lithium-ion battery anodes, Part. Part. Syst. Char. 34 (2017) 1600223.
[49] T. Xiang, Q. Fang, H. Xie, C. Wu, C. Wang, Y. Zhou, D. Liu, S. Chen, A. Khalil, S. Tao, Q. Liu, L. Song, Vertical 1T-MoS_2 nanosheets with expanded interlayer spacing edged on a graphene frame for high rate lithium-ion batteries, Nanoscale 9 (2017) 6975–6983.
[50] K. Leng, Z. Chen, X. Zhao, W. Tang, B. Tian, C.T. Nai, W. Zhou, K.P. Loh, Phase restructuring in transition metal dichalcogenides for highly stable energy storage, ACS Nano 10 (2016) 9208–9215.
[51] K. Chang, W. Chen, Single-layer MoS_2/graphene dispersed in amorphous carbon: towards high electrochemical performances in rechargeable lithium ion batteries, J. Mater. Chem. 21 (2011) 17175–17184.
[52] L. Lu, L. Zhang, H. Zeng, B. Xu, L. Wang, Y. Li, Enhanced cycling performance of Se-doped SnS carbon nanofibers as negative electrode for lithium-ion batteries, J. Alloy. Comp. 695 (2017) 1294–1300.
[53] M. Choi, S.K. Koppala, D. Yoon, J. Hwang, S.M. Kim, J. Kim, A route to synthesis molybdenum disulfide-reduced graphene oxide (MoS_2-RGO) composites using supercritical methanol and their enhanced electrochemical performance for Li-ion batteries, J. Power Sources 309 (2016) 202–211.
[54] Q. Pan, F. Zheng, X. Ou, C. Yang, X. Xiong, Z. Tang, L. Zhao, M. Liu, MoS2 decorated Fe3O4/Fe1−xS@C nanosheets as high-performance anode materials for lithium ion and sodium ion batteries, ACS sustainable chem, Eng. Times 5 (2017) 4739–4745.
[55] G. Qu, J. Cheng, Z. Wang, B. Wang, S. Ye, Self-templated formation of tremella-like MoS_2 with expanded spacing of (002) crystal planes for Li-ion batteries, J. Mater. Sci. 51 (2016) 4739–4747.
[56] B. Wang, Y. Zhang, J. Zhang, R. Xia, Y. Chu, J. Zhou, X. Yang, J. Huang, Facile synthesis of a MoS_2 and functionalized graphene heterostructure for enhanced lithium-storage performance, ACS Appl. Mater. Interfaces 9 (2017) 12907–12913.
[57] J. Guo, H. Zhu, Y. Sun, L. Tang, X. Zhang, Boosting the lithium storage performance of MoS_2 with graphene quantum dots, J. Mater. Chem. 4 (2016) 4783–4789.
[58] J. Liu, A. Fu, Y. Wang, P. Guo, H. Feng, H. Li, X.S. Zhao, Spraying coagulation-assisted hydrothermal synthesis of MoS_2/carbon/graphene composite microspheres for lithium-ion battery applications, ChemElectroChem 4 (2017) 2027–2036.
[59] D. Xie, X. Xia, Y. Wang, D. Wang, Y. Zhong, W. Tang, X. Wang, J. Tu, Nitrogen-Doped carbon embedded MoS_2 microspheres as advanced anodes for lithium- and sodium-ion batteries, Chemistry 22 (2016) 11617–11623.
[60] X. Wu, Z. Wang, M. Yu, L. Xiu, J. Qiu, Stabilizing the MXenes by carbon nanoplating for developing hierarchical nanohybrids with efficient lithium storage and hydrogen evolution capability, Adv. Mater. 29 (2017) 1607017.
[61] H. Wang, H. Jiang, Y. Hu, N. Li, X. Zhao, C. Li, 2D MoS_2/polyaniline heterostructures with enlarged interlayer spacing for superior lithium and sodium storage, J. Mater. Chem. 5 (2017) 5383–5389.